The Journal of Experimental Biology 216, 3551-3563

doi:10.1242/jeb.084699

RESEARCH ARTICLE

Force balance in the take-off of a pierid butterfly: relative importance and timing of leg impulsion and aerodynamic forces

Gaëlle Bimbard[1,*], Dmitry Kolomenskiy[2], Olivier Bouteleux[1], Jérôme Casas[1] and Ramiro Godoy-Diana[3]

[1]Institut de Recherche sur la Biologie de l'Insecte (IRBI), CNRS UMR 7261, UFR Sciences et Techniques, Université François Rabelais, 37200 Tours, France, [2]Centre de Recherches Mathématiques (CRM), Department of Mathematics and Statistics, McGill University, 805 Sherbrooke W., Montréal, QC, Canada, H3A 2K6 and [3]Physique et Mécanique des Milieux Hétérogènes (PMMH), CNRS UMR 7636, ESPCI ParisTech, UPMC (Paris 6), Univ. Paris Diderot (Paris 7), 10 rue Vauquelin, 75231 Paris, Cedex 5, France

*Author for correspondence (gaelle.bimbard@etu.univ-tours.fr)

SUMMARY

Up to now, the take-off stage has remained an elusive phase of insect flight that was relatively poorly explored compared with other maneuvers. An overall assessment of the different mechanisms involved in force production during take-off has never been explored. Focusing on the first downstroke, we have addressed this problem from a force balance perspective in butterflies taking off from the ground. In order to determine whether the sole aerodynamic wing force could explain the observed motion of the insect, we have firstly compared a simple analytical model of the wing force with the acceleration of the insect's center of mass estimated from video tracking of the wing and body motions. Secondly, wing kinematics were also used for numerical simulations of the aerodynamic flow field. Similar wing aerodynamic forces were obtained by the two methods. However, neither are sufficient, nor is the inclusion of the ground effect, to predict faithfully the body acceleration. We have to resort to the leg forces to obtain a model that best fits the data. We show that the median and hind legs display an active extension responsible for the initiation of the upward motion of the insect's body, occurring before the onset of the wing downstroke. We estimate that legs generate, at various times, an upward force that can be much larger than all other forces applied to the insect's body. The relative timing of leg and wing forces explains the large variability of trajectories observed during the maneuvers.

Supplementary material available online at http://jeb.biologists.org/cgi/content/full/216/18/3551/DC1

Key words: butterflies, take-off, variability, aerodynamic force, leg force, insect flight, flapping flight.

Received 21 December 2012; Accepted 28 May 2013

INTRODUCTION

Insects impress by their agility and their performances in flight. Understanding the aerodynamic mechanisms involved constitutes a considerable challenge for biologists and physicists, but also for engineers responsible for the design of robotics such as micro air vehicles, whose principal model is the flapping flight of insects. During the last few years, some of the characteristic kinematic patterns allowing us to explain the significant aerodynamic forces generated during flight as well as the underlying fluid dynamics have been unraveled for the many maneuvers insects display in flight. Indeed, more and more major elements of flight maneuvers such as wing kinematics and leading edge vortex production are now partially understood. This is true for hovering flight (Walker et al., 2010) as well as for forward flight (Bomphrey et al., 2006), classic subjects of insect flight studies.

By contrast, the take-off stage remains an elusive phase of insect flight as it has been relatively poorly explored compared with other maneuvers (Sunada et al., 1993; Zabala et al., 2009; Takahashi et al., 2012). However, it is a key stage, because this ground-to-air transition requires not only considerable power but also a very fast production of a significant amount of vertical force to counterbalance body weight and lift it up vertically. Furthermore, this challenge is all the more difficult as the animal has, in most cases, to generate these forces from rest, i.e. with no initial velocity. Finally, this phase is by nature highly unsteady, which hinders its experimental analysis. Mechanisms involved in this force production during take-off have thus rarely been explored in the literature.

As during the others stages of insect flight, wing aerodynamics clearly plays a major role in lift generation during take-off (Sunada et al., 1993). However, given the presence of an additional factor, i.e. the proximity of the substrate, it appears that other phenomena could be involved in the force production during take-off. Indeed, it has been highlighted and quantified, *via* a force sensor, that some birds would also rely on the extension of their legs to initiate their take-off flight from a perch or from a platform (Earls, 2000; Tobalske et al., 2004; Berg and Biewener, 2010). Similar leg extension kinematics have also been documented during insect take-off (Zabala et al., 2009), suggesting a conserved method to help vertical force production in these animals. Moreover, the presence of the substrate under the animal could also have an impact on the airflow generated by the insect motion. This ground effect, well known in the field of aviation, refers to the modification of the aerodynamic forces when the flying body is placed at a distance from a substrate of the order of one wingspan or less. The proximity of the ground leads to a decrease of the formation of wing-tip vortices and of the drag force and an increase of lift in horizontal flight (Rayner, 1991). However, these assumptions remain hypothetical in the context of insect take-off.

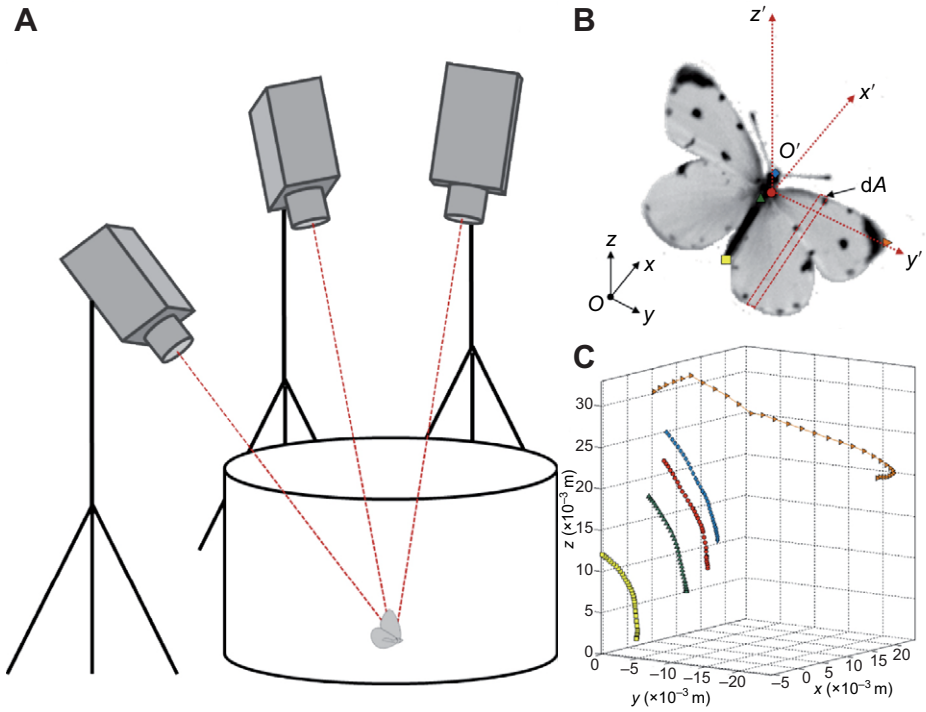

Fig. 1. (A) High-speed video recording setup. (B) Reference frames and definition of the points used for the video tracking. *Oxyz* is the frame fixed on the earth; *O′x′y′z′* is the frame fixed on the wing, with its origin at the wing root. The *y′*-axis, along which wing elements of various area d*A* follow each other, spans the wing from the root (red circle) to the tip (orange triangle). The blue diamond, the green triangle and the yellow square represent the head, the center of mass and the tip of the abdomen of the insect, respectively. (C) Tracked points in the *Oxyz* reference frame for the first half wing beat.

In this paper we examine the take-off maneuvers of butterflies from a force balance perspective. We focus on the first downstroke of *Pieris rapae* (Linnaeus 1758) (Lepidoptera: Pieridae) butterflies taking off from a horizontal flat surface. Starting from a natural position prior to take-off with both wings pointing upwards, the first downstroke starts producing the lift force that drives the ground-to-air transition. A balance of forces along the *z* direction gives:

$$m\ddot{z} = F_z(t) - mg, \quad (1)$$

where m is the mass of the insect, $\ddot{z}$ is the position of its center of mass in the global coordinate system *Oxyz*, $F_z(t)$ is the lift force and g is gravitational acceleration. We characterized in detail the wing and body kinematics during this initial stage of the take-off maneuver using high-speed video recordings and used the measurements for a double purpose. In order to determine whether the sole aerodynamic force produced by the wings could explain the observed motion of the insect body, we compared, as a first step, a rough analytical model of the force produced by the wings with the acceleration of the center of mass of the insect calculated from the video tracking of the wing and body motions. Secondly, numerical simulations of the aerodynamic flow field using the wing kinematics were carried out for flight setups assuming tethered and free flight with or without the ground effect. The ground effect is shown to play only a minor role, mainly because of the transient nature of the phenomenon. We show that the leg extension has to be taken into account as one of the main elements in the take-off force balance. The lift force in Eqn 1 can thus be written $F_z(t)=F_{az}+F_{lz}$, where F_{az} and F_{lz} are the forces produced by the wings and the legs, respectively. Using a linear compression spring model for F_{lz}, we prove that these legs forces can be active from the very beginning of the maneuver or at the same time as the peak of aerodynamic lift, in the second portion of the first downstroke. Furthermore, we performed an experiment in two ways to confirm the role of leg extension in the early phase of take-off. First, the kinematics of the different insect's limbs was reconstructed. Then, the chronology between the different major events, i.e. leg extension and wing and body motion, was recorded for the initial phase of the take-off. This was done in order to assess whether the observed leg extension was a passive mechanism occurring in response to the upward motion of the insect's body or whether the insect's limbs had an active role in lifting the body from the ground.

MATERIALS AND METHODS

Kinematic capture

Four-day-old cabbage white butterflies (*Pieris rapae*) with intact wings were selected from the rearing population at the Research Institute on Insect Biology (Tours University) on the basis of a strong flight motivation.

For recording, each insect was placed at the bottom of a white plastic flight cylinder (height: 79.5 cm; diameter: 77 cm) surrounded by three high-speed digital video cameras: two Phantom V9 cameras (Vision Research, Wayne, NJ, USA) fitted with Nikkor 24–85 mm lenses (Nikon Imaging Japan, Tokyo, Japan) and one Photron Ultima APX camera (Photron USA, San Diego, CA, USA) equipped with a Sigma 24–70 mm lens (Ronkonkoma, NY, USA) (see Fig. 1A). This design was chosen to provide three complementary points of view on the insect throughout the stroke cycles. Three 100 W spotlights were added to bring bright lighting conditions necessary to capture good quality frames. We waited for a spontaneous animal take-off to trigger the three synchronized cameras. Take-off sequences were recorded at 1000 frames s^{-1} with a resolution of 1024×1024 pixels. The cameras were calibrated using dedicated software to obtain high-resolution images of moving and deforming surfaces. The details of the calibration are described in Walker et al. (Walker et al., 2009). In brief, a bundle adjustment procedure was used to produce joint optimal estimates of (1) the camera parameters and (2) the spatial coordinates of points on a two-dimensional calibration grid for a range of positions and orientations.

When the initial resting position was not with both wings vertically pointing upwards, the take-off wing motion started invariably with a partial upstroke to bring them to this position. This first upstroke of the wings, always incomplete and different

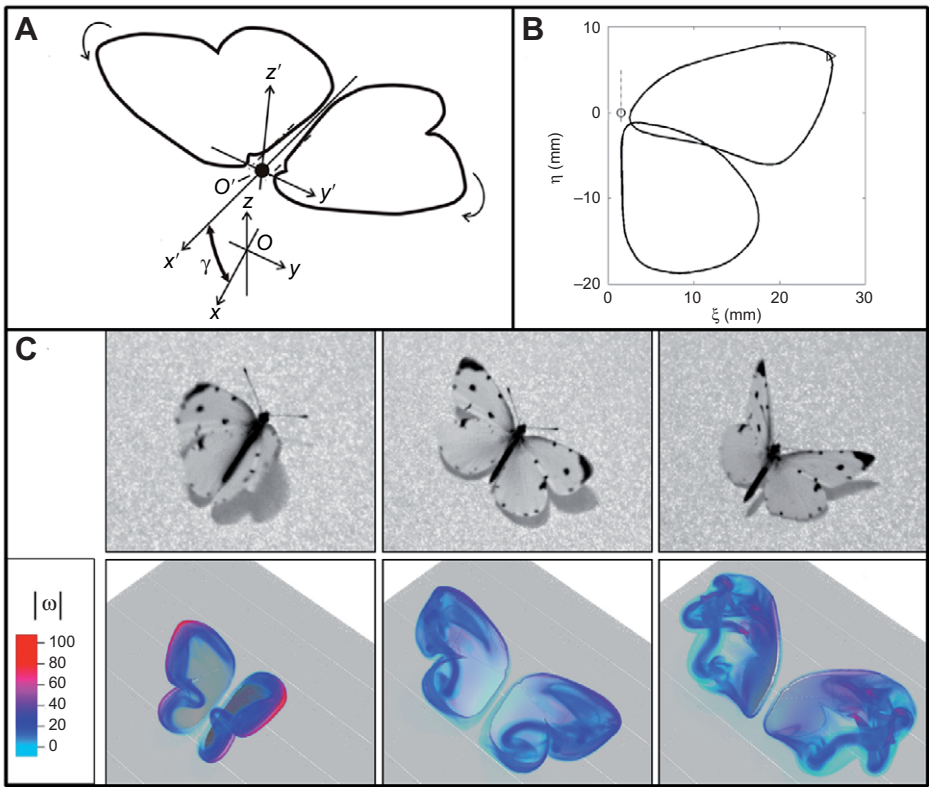

Fig. 2. Numerical simulation configuration. (A) Schematic diagram of the numerical setup. The wings are two rigid flat plates, but the contour is realistic. They rotate in opposite directions about two axes parallel to the intersection line between the two wing planes. The *x*′-axis is also parallel to the same line and the *z*′-axis is perpendicular to it. Both are in the plane of symmetry. The *y*′-axis completes the triad. The origin *O*′ is the insect's base point, the point in the middle between the two wings' roots. The wings are initially aligned with the x′z′-plane. The time variation of the angular velocity is imposed using the polynomial fit of the experimental measurements. The laboratory frame of reference *Oxyz* is such that the planes *Oxz* and *O*′*x*′*z*′ coincide. The angle between *Ox* and *Ox*′ is denoted as γ. The coordinates of point *O*′ in the frame *Oxyz* are $x=x_b$, $y=0$ and $z=z_b$. (B) Realistic wing contour obtained by digitizing a photographic image. The positions of the wing points used in the numerical simulations on the wing contour are also indicated. The root is at (ξ_R, η_R) and the tip is at (ξ_T, η_T), where ξ_R=1.5 mm, η_R=0, ξ_T=25.889 mm and η_T=6.609 mm. (C) Visualization of the vorticity field |ω| (in color), near the wings and the ground surface. Time instants are *t*=10, 20 and 30 ms. The vorticity magnitude is in cs^{-1}. Corresponding frames extracted from the video are shown above.

from one video recording to another, was not taken into account. We focus in the present analysis on the first complete downstroke period, referred to as *T*, from that first upstroke–downstroke transition to the next downstroke–upstroke transition. Furthermore, butterflies move the forewings and hindwings almost as one solid wing, thus the two are considered as a single whole wing. It is assumed that the wing movement is symmetric.

With the calibration software previously cited, a set of natural features selected on the right wing and on the body of the insect (e.g. wing tip, wing root, head, center of mass and abdomen) was manually tracked throughout that first downstroke. For each insect, we considered the center of mass as the liaison point between its thorax and its abdomen, as it has been estimated with *Pieris melete*, a closely related species (Sunada et al., 1993). We considered the center of mass at the same place on the insect's body during take-off flight and we ignored the effect of the insect's wings on its position. Indeed, its variation has very little influence on the final force balance, generating a negligible maximum inertial force (i.e. ~7% of the maximum aerodynamic force and less than 2% of the maximum force due to legs, according to our calculations). Depending on the position of the insect through its take-off flight, some of the previously mentioned points happened to be hidden from the viewpoint of at least two cameras during portions of a trial. Missing data were then estimated by cubic interpolation and completed coordinates were fitted using a simple moving average method. The obtained three-dimensional coordinates of the different points were used as described below to estimate the forces produced during the first downstroke of take-off flight. The points that will be exploited are defined in Fig. 1B using a snapshot. Their tracks on an *Oxyz* reference frame are also depicted (see Fig. 1C).

Tests of force balance

In order to quantify the balance of forces during the take-off, we estimate, from the experiments, the lift force $F_z(t)$ of Eqn 1 using the vertical acceleration. The position *z* of the center of mass in the global coordinate system *Oxyz* was plotted as a function of time and used to calculate $\ddot{z}$. In order to eliminate random fluctuations, the data were fitted with a polynomial curve of suitable degree (usually between 6 and 8) before taking its derivatives. The polynomial fit was chosen because it smooths out data more than the low-pass filters commonly used, allowing us to obtain force curves with only the major trends and so to clearly differentiate the various types of responses. Importantly, more weight has been allocated to the first 10 data points of the trials. This procedure, not possible or very difficult using filters, strongly limits the irrelevant variations in the region of interest, the initial phase of take-off.

We consider first the lift force produced by the wings only, F_{az}, which can be estimated in two different ways. As a first step, we

compute an estimate for F_{az} using a rough analytical model that gives some insight into the dynamics of force production. It is referred as F_{az}^{am} (the subscript stands for the z component of the aerodynamic lift force and the superscript stands for the analytical model). To estimate the lift force produced by the wing, we consider the dynamic pressure $\rho|\vec{u}|^2$, where ρ is the fluid density and $\vec{u}$ is the instantaneous velocity of an element of the area dA of the wing (Fig. 1B). It produces a force $d\vec{F}$ that is oriented at each instant in the direction normal to the wing surface. A reference frame with the origin at the wing base was chosen for each wing so that one of its axes is aligned with the plane of motion during the first half of the wingbeat period (see y-axis in Fig. 1B). Furthermore, the velocity of a slice of wing element can be written as $\vec{u}=y'\dot{\theta}$, considering a wing surface described by a chord that varies along the span as the function $c(y')$. Here $\dot{\theta}$ is the angular velocity of the wing, i.e. the first derivative of $\theta(t)$, the angle describing the wing motion (and the direction of the y'-axis), obtained from the kinematics measurements. The element of force projected in the direction of gravity can thus be written:

$$dF = 2\rho y'^2\dot{\theta}^2 c(y')\cos\theta\cos\gamma dy', \quad (2)$$

where γ is the angle between the x'-axis and the horizontal (see Fig. 2A) and where the element of area of the wing is written $dA=c(y')dy'$ in terms of the chord $c(y')$. Integrating along the wingspan gives the lift force as a function of time:

$$F_{az}^{am}(t) = 2\rho\dot{\theta}^2(t)\cos\theta(t)\cos\gamma\int_0^{span} c(y')y'^2\,dy'. \quad (3)$$

This analytical model for the aerodynamic lift force is compared afterwards with the value of the force obtained from numerical simulations, F_{az}^{ns} (the superscript stands for numerical simulation). Wings are considered as rigid and moving in a viscous incompressible fluid. A description of the numerical method can be found in Kolomenskiy et al. (Kolomenskiy et al., 2011). Briefly, the no-slip boundary condition at the solid boundary is modeled using the volume penalization method (Angot et al., 1999). The penalized Navier–Stokes equations are solved using a classical Fourier pseudo-spectral method, the computational domain being therefore a rectangular box with periodic boundary conditions imposed at its six faces. The time integration is exact for the viscous term and an adaptive second-order Adams–Bashforth scheme is used for the nonlinear term. Motion of the wings is treated using a Fourier interpolation technique presented in Kolomenskiy and Schneider (Kolomenskiy and Schneider, 2009). The parallel implementation of the code employs the P3DFFT fast Fourier transform package (Pekurovsky, 2012; Pekurovsky, 2013).

Three kinds of numerical simulation of increasing realism have been carried out. In this paper, they have been labeled tethered, free and free/ground simulations. The configuration is that of Fig. 2. The size of insects slightly varied between experiments but all computations were carried out assuming the same wing shapes and wing lengths L=25.3 mm. This dimension is not a mean value but that of Individual 4 (Type 1 and 3 take-offs described later). Its difference with respect to the wing length of the largest individual (Individual 7, Type 2 take-off) is only 2.7%, which is largely within the accuracy of the present simulations. It is therefore justified to use the same wing length in all simulations. The wings are modeled as two flat plates having realistic contours obtained by digitizing a photographic image. Whereas the wings extended during the first few milliseconds of the first downstroke in the experiments, the relative position of a hindwing with respect to a forewing does not change in the simulations and corresponds to a fully extended wing. One downstroke only is simulated. The angular motion of the wings is imposed using a polynomial fit to the time evolution of the positional angle θ obtained in experiments:

$$\theta = \sum_{j=0}^{7}\hat{\theta}_j t^j, \quad (4)$$

where time t is in milliseconds and the angle is measured from the $O'x'y'$ plane, in radians. The frame of reference $O'x'y'z'$ attached to the insect body is usually moving with respect to the laboratory frame of reference $Oxyz$.

The conditions of the tethered simulation correspond most closely to the simplified analytical model described below in this section. The insect is assumed to be tethered such that its body is fixed and the incidence angle is set to γ=0. The ground is not modeled. The values of the coefficients $\hat{\theta}_j$ are shown in supplementary material Table S1.

The wing shape and stroke kinematics in the free simulation are the same as in tethered simulation, but the insect is not tethered anymore. The coordinate system $O'x'y'z'$ moves such that:

$$x_b = \sum_{j=1}^{3}\hat{x}_j t^j,\ z_b = \sum_{j=1}^{3}\hat{z}_j t^j,\ \gamma = \sum_{j=0}^{3}\hat{\gamma}_j t^j, \quad (5)$$

which are polynomial approximations to the experimental measurements. In Eqn 5, time t is in milliseconds; the coordinates x_b, z_b of the insect's base point (point O′), the median point between the two wing roots, are in cm; and the angle γ between Ox and $O'x'$ is in radians. The values of the coefficients $\hat{x}_j$, $\hat{z}_j$ and $\hat{\gamma}_j$ are given in supplementary material Table S2.

Finally, the free/ground simulation further accounts for the ground effect (see Fig. 2C). A solid impermeable wall is imposed at an initial distance z_w from the base point O' (see supplementary material Table S2). This distance is approximately 1.2 to 2.2 times larger than in the experiments, but it is required to ensure that the hindwings do not touch the ground. All other parameters are similar to the case of the free simulation.

Coefficients $\hat{\theta}_j$, $\hat{x}_j$, $\hat{z}_j$ and $\hat{\gamma}$ are obtained *via* the following method of calculation. In the experiments, seven points were tracked on the insect: two on each of the left and right wings and three on the body. Only the points located on the wings were used to determine the wing kinematics for the numerical simulations. Their positions on the wing contour are indicated in Fig. 2B. The following nonlinear optimization problem was then solved: we found the polynomial coefficients of the kinematic parameters that minimize the discrepancy between the four experimental points on the wings and the corresponding points in the simulations. Because the wings were assumed to be solid, the feathering motion resulting from the wing deformation was not modeled. The experimental points as well as the corresponding points on the wings obtained by optimization are shown in supplementary material Fig. S1.

In all simulations, $\nu=1.45\times10^{-5}\,m^2\,s^{-1}$ is the ambient air kinematic viscosity. The computational domain is a rectangular box of height 5 cm and horizontal dimensions 10×10 cm. It is discretized with $N_x\times N_y\times N_z=768\times768\times384$ grid points. The parameter of the volume penalization method equals 10^{-3} cs.

In summary, three numerical simulations have been performed for take-off flights detailed later: the tethered simulation assumes a fixed and horizontal insect's body, the free simulation supposes a moving insect and the free/ground simulation represents a moving insect taking-off from the ground.

In order to investigate whether this sole aerodynamic wing force could explain the observed take-off motion, we calculated the

predicted trajectory of the insect's center of gravity (subscript cg) by integrating:

$$\frac{d^2x_{cg}}{dt^2} = F_{ax}^{ns}\ ,\ \frac{d^2z_{cg}}{dt^2} = F_{az}^{ns} - mg\ , \tag{6}$$

using the aerodynamic forces F_{ax}^{ns} and F_{az}^{ns} obtained in the numerical simulations, the motions along the *y*-axis being negligible. All computations were carried out using the same masses as in the experiments. The initial position was set to $x_{cg}(0)=z_{cg}(0)=0$ and the initial velocity $\dot{x}_{cg}(0)$, $\dot{z}_{cg}(0)$ was set to the values obtained in the experiments. If the predicted trajectory is too different from the observed one, other forces have to be involved. Comparing the experimentally measured position of the body and the insect trajectory obtained by integration, some additional force, probably due to leg extension, needed to be incorporated to obtain a faithful representation (see Results).

To model the dynamics of the force generated by the insect's legs, we assumed that all six legs act as a single linear compression spring. When fully extended, its rate is K_l and its length is L_l. Initially, it is compressed. When it is released at time t_l, it pushes against the ground surface with an angle ϕ_l with respect to the horizontal. The two components of the leg force at time $t>t_l$ are:

$$\begin{aligned} F_{lx} &= [L_l - z(t) + z(t_l)]K_l\cos\phi_l\ , \\ F_{lz} &= [L_l - z(t) + z(t_l)]K_l\sin\phi_l\ , \\ &\text{if } L_l - z(t) + z(t_l) > 0\ , \end{aligned} \tag{7}$$

otherwise

$$F_{lx} = F_{lz} = 0\ .$$

We thus added these two estimated components of leg force to the right-hand side of Eqn 6, yielding:

$$\frac{d^2x_{cg}}{dt^2} = F_{ax}^{ns} + F_{lx}\ ,\ \frac{d^2z_{cg}}{dt^2} = F_{az}^{ns} + F_{lz} - mg\ , \tag{8}$$

allowing us to obtain the time evolution of $x_{cg}(t)$ and $z_{cg}(t)$. The unknown model parameters K_l, ϕ_l and t_l (see Eqn 7) were also determined by solving a non-linear least squares problem, such as to minimize the discrepancy between the computed and the experimental trajectories, using the MATLAB Optimization Toolbox (The MathWorks, Natick, MA, USA). This resulted in the values shown in supplementary material Table S3. The leg extension length L_l=0.31 cm was estimated from video recordings and was assumed to be invariant in all take-offs. It was assumed that the legs support the body weight ($F_{lz}=mg$) during $0\leq t\leq t_l$, unless otherwise stated.

Leg motion dynamics

The tested individuals were put on a fine plastic wrap stretched at half-height of a transparent plastic box (40×25×30 cm, height × width × depth), perpendicular to a high-speed digital video camera (Phantom V9) equipped with a macro lens (AF Micro Nikkor 60 mm) placed outside the box. Two 250 W spotlights positioned above the box illuminated this arrangement. When the insect spontaneously took off, the camera was triggered and the take-off sequence was recorded at 1000 frames s^{-1} with a resolution of 600×800 pixels. The recorded sequences were then calibrated and analyzed using Didge tracking software (version 2.3; Alistair Cullum, Creighton University, Omaha, NE, USA). For each frame of videos, the insect's head (representing the insect's body), its wing tip and points defined by the different joints of the legs were manually digitized. Four points on each of the three visible legs were used to calculate the dynamics of the angles defined by the femur and the tibia (Angle 1) and by the tibia and the tarsus (Angle 2) (see Fig. 3). Only data from the visible side of the insect are used, once again assuming a symmetrical movement during take-off. In all cases, the take-off wing motion started with a partial upstroke to bring wings vertically pointing upwards. The first partial upstroke, as well as the following wing downstroke, was taken into account in the following analysis. The dynamics of the angles was time aligned with the body velocity and the wingbeat phases, calculated *via* the two-dimensional coordinates of the head and the wingtip of the insect, respectively. The instants at which each major event of take-off flight (body and wing motions, leg extension) was initiated in relation to each other were then recorded.

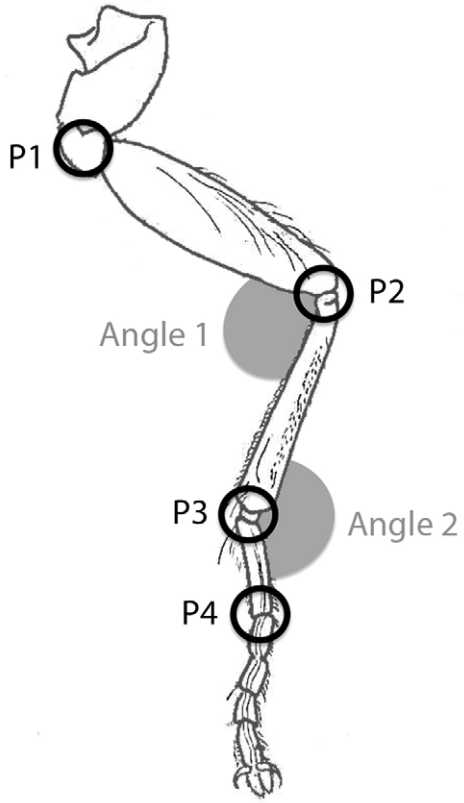

Fig. 3. Tracked points and measured angles on an insect's leg. On each of the three visible legs, the points P1, P2 and P3, and the points P2, P3 and P4 were used to calculate the dynamics of the angles defined by the femur and the tibia (Angle 1) and by the tibia and the tarsus (Angle 2), respectively.

RESULTS

Test of force balance

Altogether, 12 individuals were filmed. Only videos in which the insect took off without contact between wing and ground were selected. Among them, sequences in which the insect's body and four wings were captured by at least two cameras for the first complete stroke cycle were chosen to perform the complete analysis of wing and body kinematics. This amounted to 12 different take-offs from seven individuals (supplementary material Tables S4, S5). After presenting a typology of the take-off maneuvers in three different types of kinematics, we analyze one type in depth, thereby selecting the most important features, and end this section with a comparative analysis of the three types.

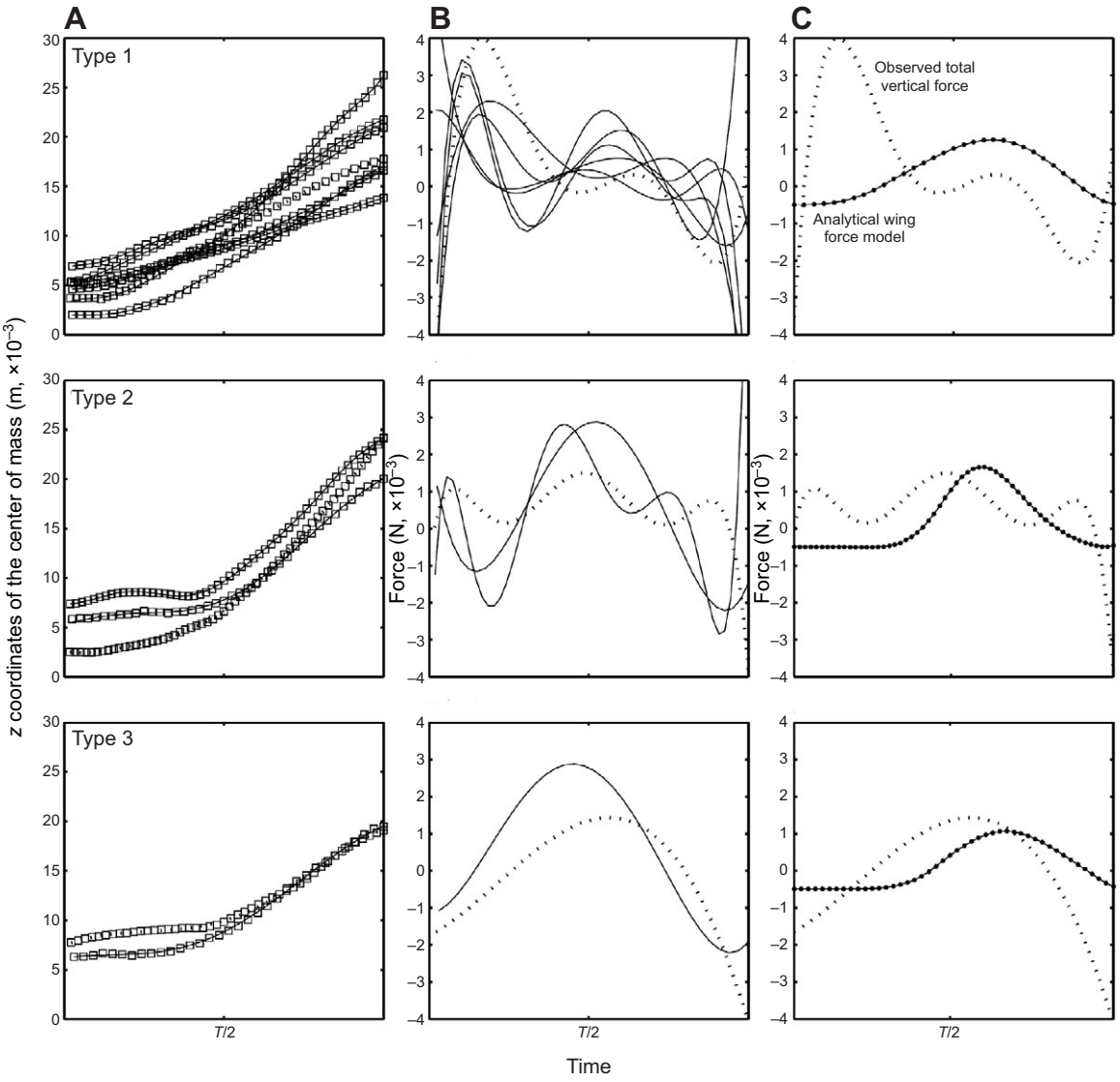

Fig. 4. Three distinct types of take-off flights (Type 1–Type 3) revealed by the analyses of the insect's body kinematics. *T* represents the downstroke period and *T*/2 marks the mid-downstroke. (A) Evolution of the experimental *z* positions of the insect's center of mass for each of the 12 take-off flights. The markers represent the original data while the lines are the fitted curves. The dotted line represents the experimental trajectory selected in each take-off type for further analyses. (B) Observed total vertical forces during take-off maneuvers. The curves represent the total vertical forces computed from observed trajectories ($m\ddot{z}$) for each of the 12 maneuvers. The dotted line represents the force pattern selected in each take-off type for further analyses. (C) Evolution of vertical forces during three specific take-off flights representative of each distinct type of maneuver. The dotted lines represent the total vertical force acting on the insect ($m\ddot{z}$) while the lines punctuated by points show the wing force obtained from solving the simple analytical model. See the Materials and methods for Eqn 3 of the wing force model.

Typology of take-off maneuvers

For all tested individuals, the total vertical force during take-off ($m\ddot{z}$) has been calculated from the time-resolved measurement of the position of the insect's center of mass *z*. All the body trajectories and the forces observed during take-off flights are grouped together in Fig. 4A,B. Three distinct patterns of force profile have been classified depending on the relative amplitude of the first and second force peaks. Indeed, the observed insect acceleration displays variability in its main traits: while a force peak always appears around mid-downstroke, another peak can be observed, only in Type 1 and Type 2 take-offs, during the first milliseconds of take-off flight. The first type (N=7) presents an early peak of high amplitude (ratio of peak 1/peak 2 >1), the second type (N=3) displays a first spike of small amplitude (ratio peak 1/peak 2 <1) while the third type (N=2) does not exhibit any secondary peak (ratio of peak 1/peak 2=0). For each of the three types of take-off maneuvers, only one particular take-off flight for a specific individual has been described and analyzed in detail *via* the different approaches later in this work. The three selected maneuvers are shown in Fig. 4C.

Detailed analysis of Type 1 take-off

In this section, we analyze in depth one take-off flight, representative of the most frequently observed maneuvers (Type 1 take-off). We first test the analytical force balance, then present the numerical simulations and end the section by incorporating the extension of legs in the force balance.

The evolution of vertical body position and progression of the net vertical force production throughout the first downstroke of

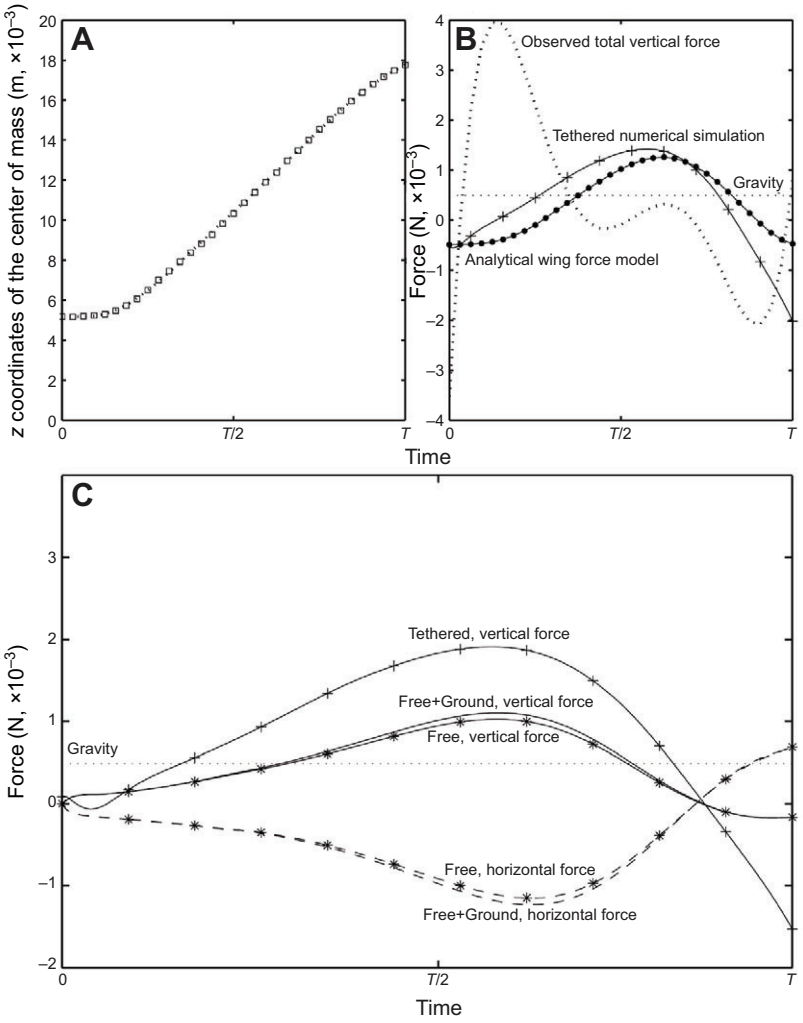

Fig. 5. Time evolution of the forces acting on the insect's body throughout the first downstroke of take-off flight of Type 1. *T* is the downstroke period. Here *T*=33 ms. (A) Evolution of the experimental *z* positions of the insect's center of mass. The markers represent the original data while the line is the fitted curve. (B) Evolution of the net vertical forces produced during take-off flight. The dotted line represents the evolution of the total vertical force actually acting on the insect ($m\ddot{z}$) while the curve punctuated by points symbolizes the analytical wing force model, calculated using Eqn 3. The black line punctuated by crosses represents the tethered numerical simulation. (C) Numerical simulations. Both horizontal and vertical components of the total aerodynamic force of the two wings obtained in the tethered, free and free/ground numerical simulations are shown. The gravity force *mg* is also presented for reference.

take-off flight is shown in Fig. 5A,B for a specific individual. The evolution of the observed total vertical force ($m\ddot{z}$) reaches its maximum value early on. This is explained by the fast increase of the *z* position of the insect's center of mass at the beginning of the downstroke. The vertical velocity [slope of $z(t)$ in Fig. 5A] of the insect's body remains thereafter practically constant through a major part of the downstroke, accounting for the pattern observed at the level of the vertical force produced. Thus, after reaching its peak, the force decreases strongly and remains stable around 0. However, a second peak value is observable shortly after *T*/2. The *z* position of the insect's center of mass then tends to increases linearly, the total force becoming consequently negative.

The analytical wing force minus *mg* [$F_{az}^{am}(t)$–*mg*] is rather different because it is negative from the beginning of the downstroke and all along the first third of the period. This indicates that the wing force is not able to counterbalance the insect's body weight and to move it up (Fig. 5B). During most of the remaining fraction of the downstroke, this wing-driven force is positive. It is during this period, and shortly after *T*/2, that the curve reaches its maximum value. It decreases then rather quickly to attain negative values just before the end of the downstroke.

The tethered numerical simulation most closely corresponding to the analytical wing force model described in the 'Tests of force balance' section of the Materials and methods (fixed center of gravity, zero body incidence angle) is also shown on Fig. 5B. The global behavior of the two curves is similar. Indeed, starting from the same value, both reach similar maximal values a few instants after the mid-downstroke.

The time evolution of the aerodynamic forces calculated in the three different numerical simulations is shown in Fig. 5C. For a better understanding of the take-off mechanism, both horizontal and vertical forces, when different from zero, are presented in this section. No significant horizontal force is generated in the tethered simulation. Therefore, only the vertical force is displayed. It is slightly negative early on, a period that, in fact, belongs to the end of the upstroke. Later, it increases almost linearly until it reaches its maximum shortly after *T*/2. It then decreases and becomes negative a few instants before the end of the downstroke, because of the acceleration reaction. Both horizontal and vertical force components are present, due to the non-zero incidence angle γ in the free and free/ground simulations. The results of these two simulations differ only slightly. Meanwhile, the motion of the center of gravity and the body inclination, taken into account in these two more realistic numerical simulations and shown in supplementary material Fig. S1, have a major influence on the time evolution of the aerodynamic forces. Indeed, the maximal vertical force in those cases is approximately half of the force generated by the tethered model. It is also approximately double the gravity force. Because of the large incidence angle, the horizontal component is of the same order of magnitude as the vertical one, and their ratio increases as the incidence angle becomes larger.

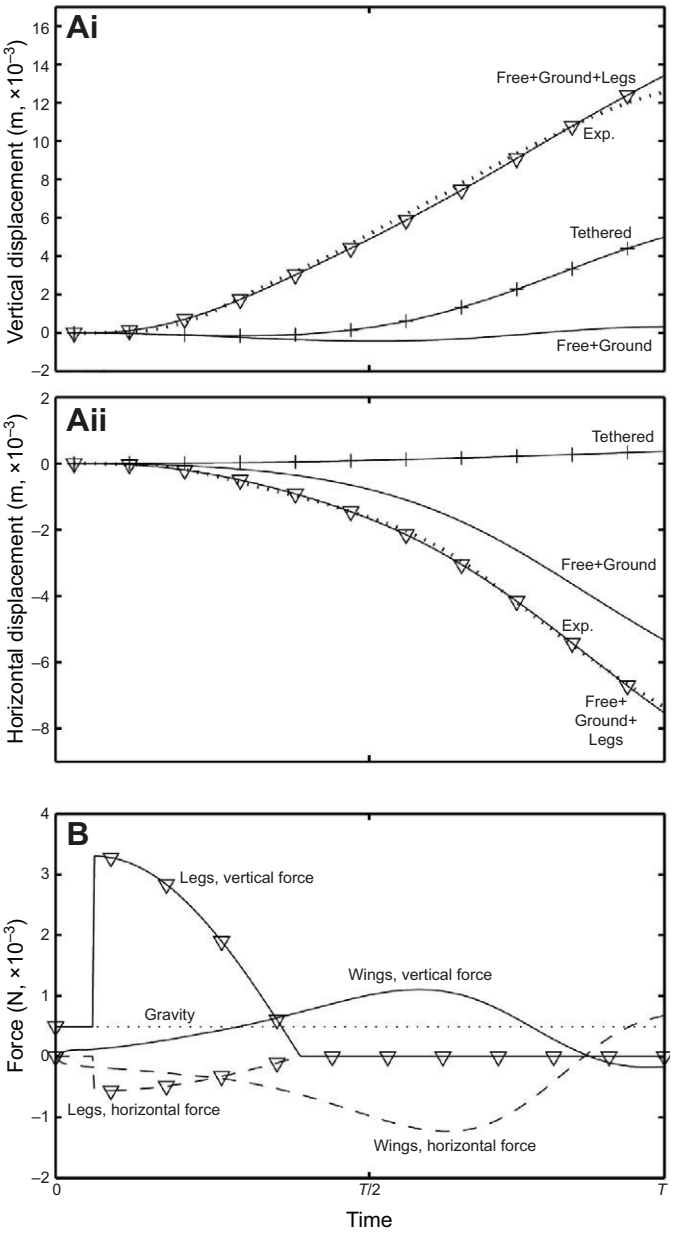

Fig. 6. Type 1 take-off: force integration from numerical simulations and leg forces. (A) Time evolution of the vertical (i) and horizontal (ii) position of the insect's center of gravity, calculated using Eqns 6 and 8. The observed insect's trajectory is also represented for comparison and is referred to as Exp. (B) Time evolution of the forces acting on the insect's body during the take-off. Both vertical and horizontal components of the force generated by the legs, calculated using Eqn 7, and of the total aerodynamic force of the two wings obtained in the free/ground numerical simulation are shown. The gravity force *mg* is also presented for reference. Here T=33 ms.

After having shown that the numerical simulations and the analytical model do match rather well, we now test whether the integration of the forces in the numerical simulations does reproduce the observed body kinematics. Fig. 6A shows the time evolution of z_{cg} and x_{cg} calculated using the forces from the tethered and the free/ground simulations. Being an intermediate case, the results obtained with the free numerical simulation are not shown. The vertical coordinate obtained integrating the force from the tethered simulation slightly decreases at the beginning of the downstroke, because the aerodynamic force is not sufficient to support the body weight. Later, it slowly increases and the insect gains 5 mm of altitude by the end of the downstroke. No significant horizontal motion happens because the horizontal force in the first case is very small. For the free/ground simulation, the insect only gains 0.5 mm of altitude by the end of the downstroke, the aerodynamic vertical forces generated being lower than the forces produced in the tethered model.

Both tethered and free/ground numerical simulations deviate from the observed insect's trajectory just after the beginning of the downstroke. Indeed, by looking at the experimentally measured position of the body (Fig. 6A), we notice that the slope of $z_{cg}(t)$ suddenly increases very early on and remains almost constant until the end of the downstroke. The additional forces involved at the onset of the take-off are assumed to be produced by the legs. They are obtained using the linear compression spring model (Eqn 7), the results of which are shown in Fig. 6B, depicting the time evolution of F_{lx} and F_{lz}. Aerodynamic forces F_{ax}^{ns} and F_{az}^{ns} are also shown for reference. The peak is asymmetric and the leg force is discontinuous. The corresponding time evolution of x_{cg} and z_{cg} is shown in Fig. 6A. The agreement with the experimental measurements is much better, showing that the work done by the legs must be included.

Comparative analysis of different types of take-offs

Again, we focus on a specific take-off flight for a particular insect for each of the Type 2 and Type 3 maneuvers. A comparison including the previously analyzed Type 1 is also made.

The evolution of the net vertical force production throughout the first downstroke of take-off flights of all three types was already shown in Fig. 4C. For both Type 2 and Type 3 take-off flights, the evolution of the observed total vertical force acting on the insect ($m\ddot{z}$) is quite different from the evolution of the wing force. It is also very different from the pattern of the total force acting on the insect during the maneuver observed for Type 1. In the case of take-off for Type 2, the total vertical force is positive most of the time. A first peak, of low amplitude, is observable just after the beginning of the period while the maximum value is reached later, around the mid-downstroke. A last peak is attained just before the end of the downstroke, when the total force becomes definitely negative. The vertical force acting on the insect displays a different pattern during Type 3 take-off flight. Indeed, the curve is negative during the first quarter of the downstroke and becomes positive to reach its maximum value right after mid-downstroke. Just before the end of the downstroke, the vertical force becomes negative again.

In Types 2 and 3, the analytical wing force model minus *mg* [$F_{az}^{am}(t)$–*mg*] shows approximately the same evolution as the wing force produced by the insect during take-off Type 1 flight. Indeed, it takes negative values throughout the first third of the period and becomes positive during the second third (Type 2) and for most of the downstroke in Type 3. The curves reach their maximal values shortly after $T/2$ and then decrease to turn negative a few instants before the end of the downstroke.

Only results obtained with the free/ground numerical simulation considered in the previous sections are presented in this section for Type 2 and 3 take-offs. Furthermore, only vertical forces, more interesting in our case, are shown for these two types of take-offs. Fig. 7A depicts the time evolution of forces acting on the insect during the three types of take-off flights. As compared with the previous case (Type 1), the estimated force generated by the legs during the Type 2 maneuver is 25% smaller, while the maximum aerodynamic force is just slightly lower. In addition, the downstroke takes almost twice as much time. However, the relative positions of the two peaks of the forces are nearly the same as during the Type 1 take-off. The sum of the two forces results in a double-peak

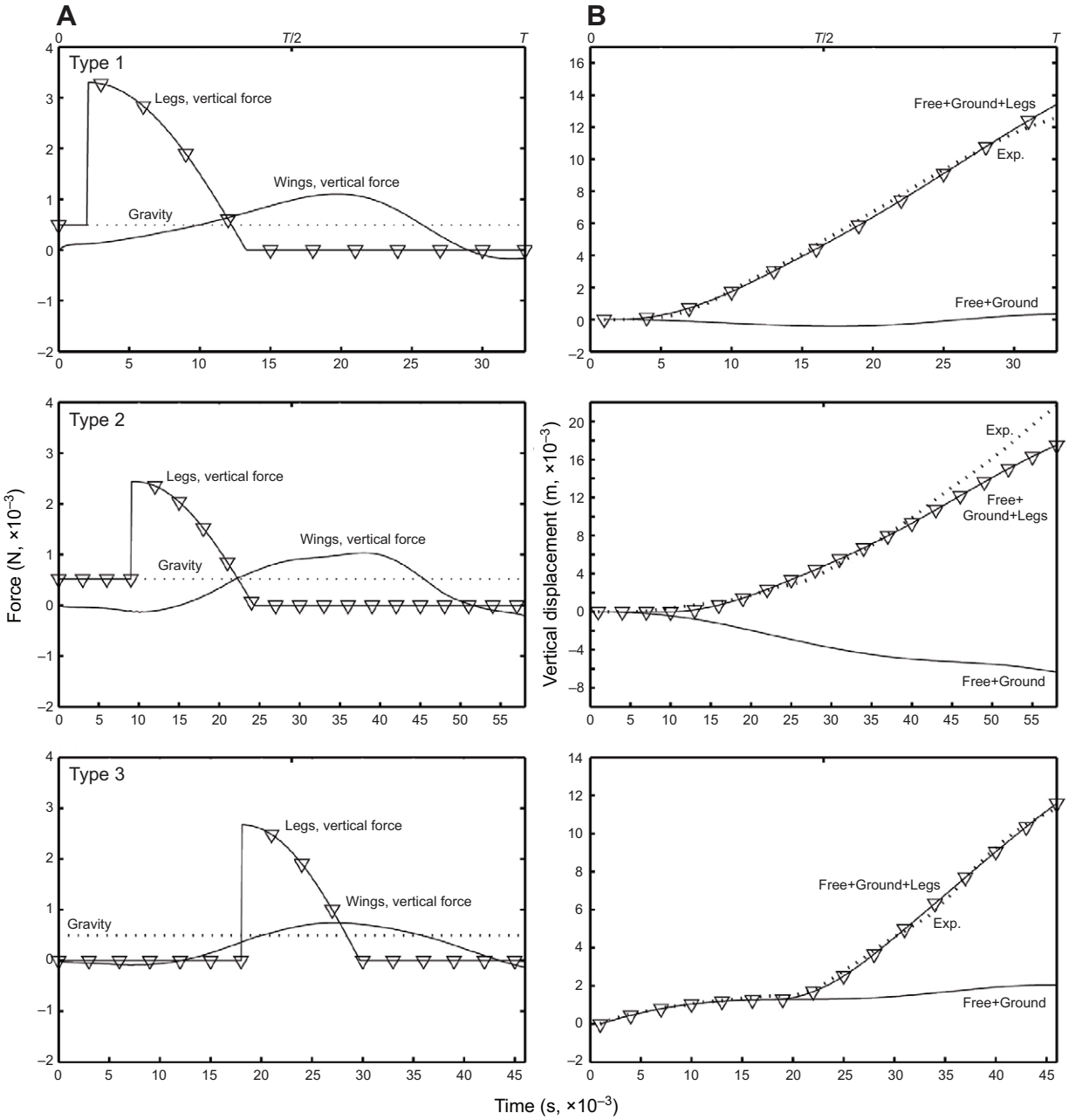

Fig. 7. Leg forces and force integration from numerical simulations in all three types of take-off. (A) Time evolution of the vertical forces acting on the insect's body during the three different types of take-off. The vertical components of the force generated by the legs, calculated using Eqn 7, and of the total aerodynamic force of the two wings obtained in the free/ground numerical simulation are shown. The gravity force *mg* is also presented for reference. (B) Time evolution of the vertical position of the insect's center of gravity, calculated using Eqns 6 and 8. The observed insect's trajectory is also represented for comparison and is referred to as Exp. The downstroke time in milliseconds is also shown here for each take-off type.

curve similar to that observed in the experiments. The time evolution of the position of the center of gravity during the Type 2 take-off, displayed with the two other types in Fig. 7B, shows the need to account for the estimated force generated by the legs. Unlike in the two cases of Type 1 and Type 2 take-offs, the initial velocity of the center of gravity for the Type 3 take-off is non-zero: $\dot{x}_{cg}(0)$=–0.06 m s^{-1} and $\dot{z}_{cg}(0)$=0.165 m s^{-1}. The maximum aerodynamic force is only slightly larger than the weight. The large vertical acceleration at t=20 ms must therefore be attributed to the extension of the legs. In contrast to the previous take-off types, this leg impulsion, referred to as a jump, occurs in the middle of the downstroke, when the aerodynamic force is near its maximum. The maximum F_{lz} is 3.5 times as large as F_{az}^{ns} in this case. Possibly, the insect first jumped before t=0, but with an effort insufficient for a take-off. This could explain the non-zero initial velocity (for this reason we assumed that the legs produce zero force during $0 \le t \le t_l$). The sum of all external forces acting on the insect during the downstroke results in a single-peak time evolution.

Leg motion dynamics

Five recordings for each of four insects were chosen for further analyses, based on video quality and the insect's initial position.

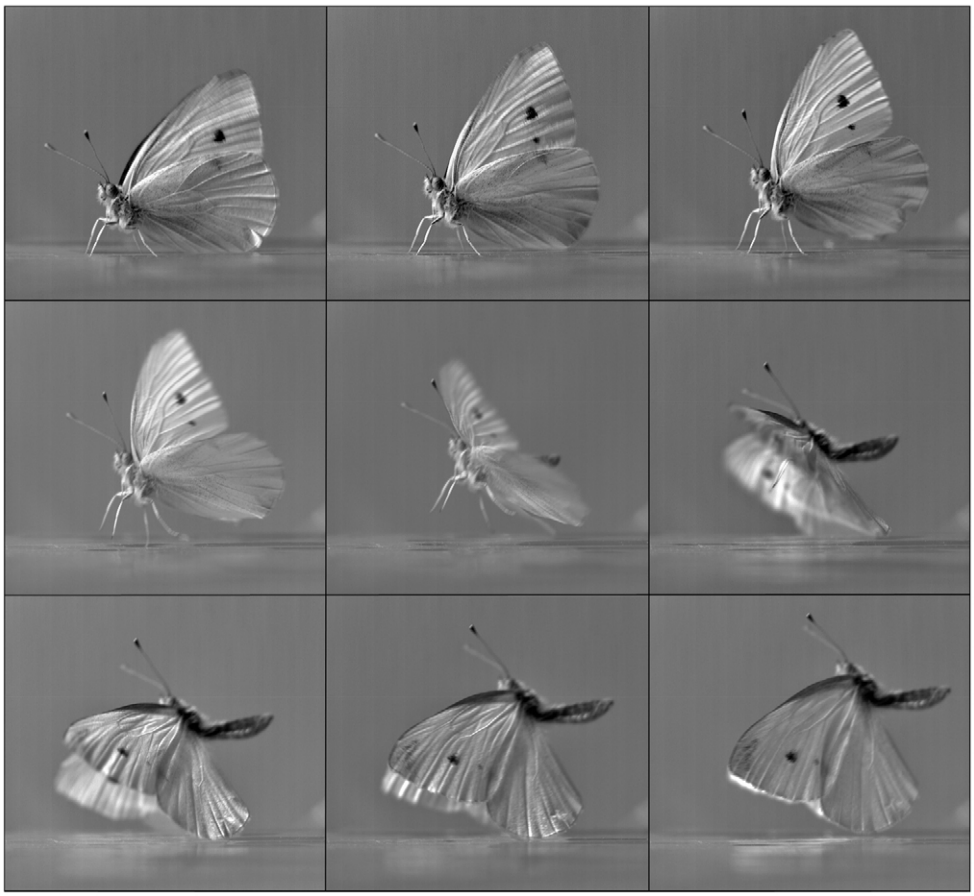

Fig. 8. Successive instants in the first wingbeat of the take-off maneuver of the butterfly *Pieris rapae*. The selected frames show every 5 ms from the first upstroke–downstroke transition to the end of the first downstroke of take-off flight.

Some frames extracted from a typical take-off sequence are shown in Fig. 8.

The dynamics of the angle defined by the femur and the tibia of the median and hind legs of the insect during take-off flight is depicted in Fig. 9A. This angle increased from 0.165 to 0.61 rad for the hind leg, and from 0.46 to 1.6 rad for the median leg in only 18 ms. By contrast, no clear trend emerged concerning that angle for the front leg. It decreased in some cases and stayed constant otherwise. The angle defined by the tibia and the tarsus of each of the three legs does not change over time, staying confined at a value around 3 rad throughout the take-off flight. The front legs did not take part in the maneuver, remaining folded under the insect's thorax all along.

The timing of the different major events of take-off flight relative to the onset of body motion is represented in Fig. 9B. The wing is first to initiate its motion, with its upstroke (−10.85 ms). Shortly after that, the hind legs (−8.2 ms), followed by the median legs (−6.89), start to extend. The body begins to move up only a few instants later. We observed a large deformation of the plastic surface under the animal just after the beginning of the leg extension, corresponding to the instant when the insect's body begins to move up in all sequences. The wing downstroke occurs much later, 13.75 ms after the onset of body motion.

DISCUSSION

We have studied the take-off maneuver of the *P. rapae* butterfly in detail. The measurements reported here enabled us to quantify the different physical mechanisms involved in the equilibrium of forces.

Two different approaches, analytical and computational, estimated the aerodynamic force produced by the wings during the first downstroke of the take-off phase. In spite of the rough character of the simple analytical model for the aerodynamic force $F_{az}^{am}(t)$, it captures the essential features of the force curve obtained with the tethered numerical simulation of the full Navier–Stokes equations remarkably well. Concerning the aerodynamic force produced by the insect, we observed that the evolution of wing force production seems relatively consistent in all types of take-off flights. Its dynamics, reaching a maximum around mid-downstroke, is furthermore consistent with measured and predicted data previously obtained for butterfly take-off (Sunada et al., 1993). As may be observed in the case of Type 1 take-off, the simple analytical model for the aerodynamic force $F_{az}^{am}(t)$ and the corresponding numerical simulation of the full Navier–Stokes equations reach similar maximal values, just after mid-downstroke. These estimates appear to be in agreement with those highlighted in 1987 by Marden, who observed a maximum lift production reaching 0.14×10^{-2} N during the take-off phase in *P. rapae* (Marden, 1987). However, the more realistic free and free/ground numerical simulations predicted force values half of those predicted by our analytical model, revealing the considerable influence of body motion and body inclination on aerodynamic forces.

To our knowledge, this study is also the first test of the influence of the ground effect on force production during take-off flight in insects. This aerodynamic mechanism has already been shown to increase lift in organisms and vehicles swimming or flying near a substrate (Tanida, 2001). It has notably been studied in various bird species, organisms that seem to use this phenomenon to minimize

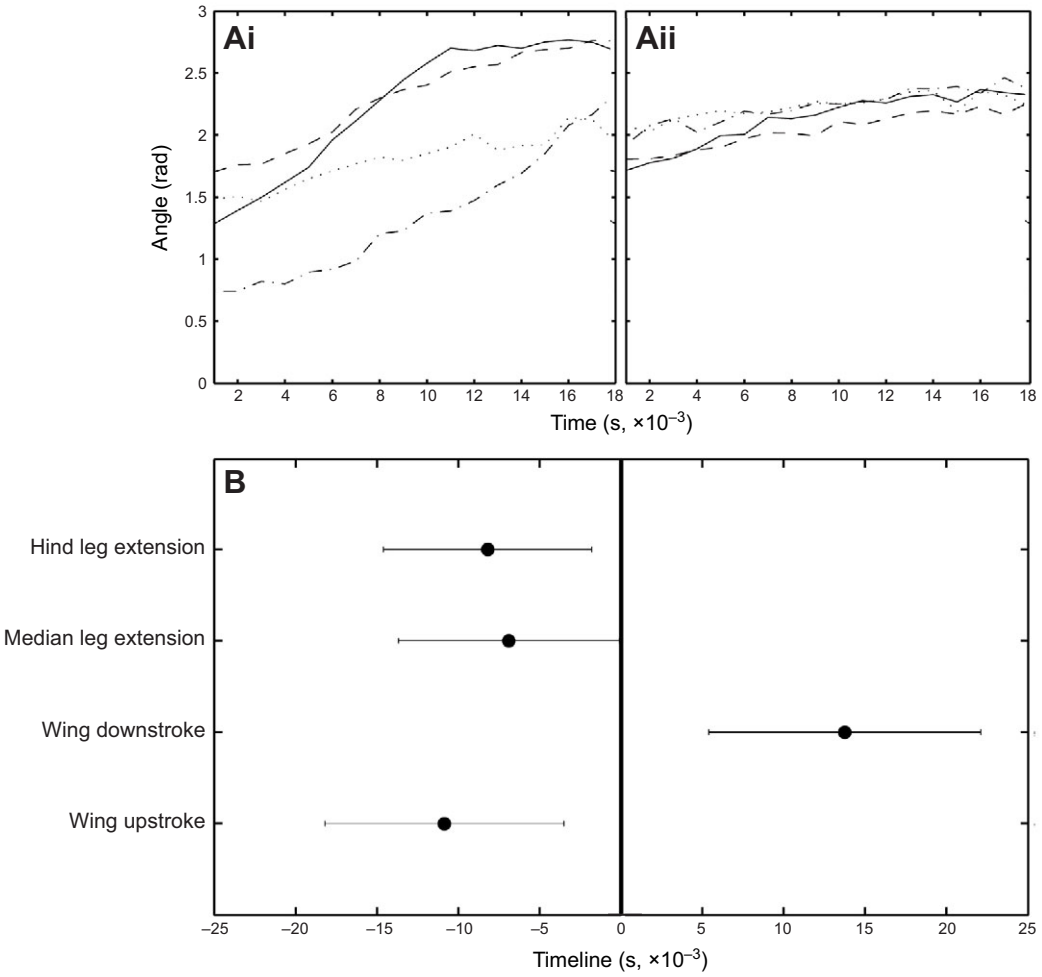

Fig. 9. Leg motion dynamics along take-off flight. (A) Evolution of angle 1 of each of the median (i) and hind (ii) legs of the insect during take-off flight. Each curve represents the mean angle of five recorded sequences for a specific individual. Time 0 has been defined as the instant when the angles began to increase. (B) Chronology of the different events of a take-off flight. The vertical line at x=0 represents the initiation of upward body motion. Values of the different events initiations are means ± s.d.

energy expenditure during flight (Finn et al., 2012). However, in our case, the results of the two simulations, with and without ground effect, differ only slightly. The conclusion is that the ground effect is unimportant for the take-off maneuver considered here. Indeed, even though the body is near the ground during the early stage of the downstroke, the wing tips that produce most of the force never approach the ground surface because of the body motions.

This work points out the importance of leg forces in the take-off maneuver. Indeed, during Type 1 take-off, the rapid change of the insect's velocity observed in the experiments requires a large force pulse localized at the beginning of take-off flight. Aerodynamic forces are small at that stage. Hence, as no other external forces are applied to the insect's body, the large pulse can only be attributed to the reaction produced by the legs pushing away from the ground. A force peak due to leg extension has been invariably observed in all three types of take-off flights, supplementing the vertical force produced by the insect wings. This upward force is, at some point in time, much larger than all other forces applied to the insect's body. The legs action is shorter in time compared with the aerodynamic force, but the peak is much larger. Indeed, the legs force is estimated to be as large as five times the body weight for Type 2 take-off flight, but can reach values up to seven times the insect weight in the case of Type 1 take-off flight. In addition to its magnitude, the timing of this force pulse is also quite variable. This can be seen, for instance, comparing the relative positions of the two force peaks during the three different types of maneuvers. Concerning the Type 1 and the Type 2 take-offs, the legs act before the wings can produce any significant lift. By contrast, the jump occurs in the middle of the downstroke during Type 3 take-off flight, when the aerodynamic force is near its maximum. The large upward force generated by the legs can be explained by their kinematics, as highlighted in our leg motion dynamics experiment. We showed that the upper parts of the median and hind legs extend largely during the maneuver. By contrast, the angle between the tibia and tarsus did not vary. This might ensure some stiffness of the lower part of the legs and an efficient transmission of energy to the ground during the propulsion. If the extension were a passive mechanism, the increase of the leg angles would start either at the same time as or just after the upward body motion. This experiment thus strongly confirms an active impulsion by the legs, the rise of the insect's body being initiated in most cases by the limbs before the onset of the wing downstroke, the only phase of the wingbeat capable of producing an upward force. The absolute values of the timing sequences of the leg kinematics cannot be directly compared with the delays estimated in the remainder of the study because of the different setups. In particular, the thin flexible plastic foil used for visualizing the onset of the leg impact on the ground surface might have had unexpected effects on these aspects of the initial take-off phase.

Although very few data are available for insects, the essential role of legs in the take-off maneuver has already been observed for birds. In particular, hindlimbs have been proved to contribute up to 25% to total velocity during take-off in the pigeon *Columbia livia* (Berg and Biewener, 2010), 93% in finch and 95% in dove (Provini

et al., 2012). In the quail *C. coturnis* and the starling *S. vulgaris*, in which hindlimbs seem contribute up to 88 and 91%, respectively, to the initial velocity, the leg force production could attain approximately four up to eight times the body weight during take-off. Despite their spindly legs, forces of similar orders of magnitude have been obtained here for *P. rapae*, revealing leg force values close to the eight times reported for locusts during the jump maneuver (Burrows, 2003). The difference of mass between the two species could explain these impressive results (2 g for locusts *versus* 50 mg for butterflies). An anatomical feature already highlighted in others insects with delicate legs, such as *Drosophila melanogaster*, could also be at play. In that insect, the tergotrochanteral muscles in the mesothoracic segment play a major role, providing the force to propel a fly from the substratum during the initial jumping phase of the take-off behavior (Allen et al., 2006). This kind of jumping mechanism has been identified in a variety of insects, including shore bugs and jumping plant lice, where the main propulsive forces are applied to the trochantera by depressor muscles located in the thorax (Burrows, 2009; Burrows, 2012). In these cases, the power-producing muscles contract slowly before a jump, the energy being stored in structures within the body and released suddenly. Moreover, ongoing work on a moth species shows that they are also quite capable of jumping in the air (M. Burrows, personal communication). Concerning the timing of leg force production, those peak forces have been shown to occur at various instants during take-off flight of organisms previously mentioned: while the starlings perform a counter-movement jump followed by wing movement to initiate the maneuver, the quail makes a squat jump responsible for a peak force with simultaneous wing movement (Earls, 2000). The force timing pattern has also been highlighted as being dependent on external conditions (i.e. voluntary take-off *versus* escape maneuver) in hummingbirds (Tobalske et al., 2004) and in *Drosophila* (Card and Dickinson, 2008). However, this possibility is excluded in our case by the standardized experimental conditions.

The legs' extension could ensure that the animal's body is raised high enough above the substrate to enable a full wing stroke without touching the ground (Heppner and Anderson, 1985). It has also been proposed that the hindlimbs work to aid lift production during take-off, increasing airflow over the wings, notably by running (Rüppell, 1975). Leg work seems thus to be of major importance in the take-off maneuver of several groups of flying animals and to operate through different dynamical mechanisms. The results of the present study show that butterflies indeed rely on this force as a crucial component of the take-off force balance, in particular driving the initial acceleration when the aerodynamic force is not yet fully available.

LIST OF SYMBOLS AND ABBREVIATIONS

c	wing chord
$\mathrm{d}A$	area of an element of the wing
$\mathrm{d}F$	vertical component of the wing element force
F_{ax}	horizontal component of the aerodynamic lift force produced by the wings
$F_{\mathrm{ax}}^{\mathrm{am}}$	horizontal component of the wing lift force calculated with the analytical model
$F_{\mathrm{ax}}^{\mathrm{ns}}$	horizontal component of the wing lift force obtained from numerical simulations
F_{az}	vertical component of the aerodynamic lift force produced by the wings
$F_{\mathrm{az}}^{\mathrm{am}}$	vertical component of the wing lift force calculated with the analytical model
$F_{\mathrm{az}}^{\mathrm{ns}}$	vertical component of the wing lift force obtained from numerical simulations
F_{lx}	horizontal component of the leg force
F_{lz}	vertical component of the leg force
$F_z(t)$	lift force
g	acceleration due to gravity
K_{l}	spring compression rate of the legs
L	wing length
L_{l}	leg extension length
m	mass of the insect
$Oxyz$	global coordinate system
$O'x'y'z'$	wingbase-referenced coordinate system
t	time
T	downstroke period
t_{l}	spring releasing time
$\vec{\mathrm{u}}$	instantaneous velocity of an element of the wing
x_{b}	x coordinates of the insect's base point
x_{cg}	x coordinates of the insect's center of gravity
z_{b}	z coordinates of the insect's base point
z_{cg}	z coordinates of the insect's center of gravity
z_{w}	initial vertical distance between the insect's base point and the ground
γ	incidence angle
θ	positional angle of the wing
ν	air kinematic viscosity
ρ	fluid density
ϕ_{l}	angle formed by the leg of the insect and the horizontal

ACKNOWLEDGEMENTS

We thank Richard Bomphrey and Simon Walker from the Department of Zoology, Oxford University, for providing us the analysis software. D.K. thanks Hao Liu and Masateru Maeda for useful comments. Imagery in Fig. 2C was produced using VAPOR, a product of the Computational Information Systems Laboratory at the National Center for Atmospheric Research (Clyne et al., 2007).

AUTHOR CONTRIBUTIONS

G.B. collected and analysed all data, and produced the first draft of the paper. D.K. carried out the numerical simulations and designed the leg force model (Eqn 7). O.B. participated in the leg kinematics experiment design, and collection and analysis of the data. J.C. participated in the design of the study and the writing of the manuscript. R.G.-D. designed the analytical force balance, participated in the design of the overall study and in the writing-up phase.

COMPETING INTERESTS

No competing interests declared.

FUNDING

This work was financially supported by the French National Research Agency [ANR-08-BLAN-0099].

REFERENCES

Allen, M. J., Godenschwege, T. A., Tanouye, M. A. and Phelan, P. (2006). Making an escape: development and function of the *Drosophila* giant fibre system. *Semin. Cell Dev. Biol.* **17**, 31-41.

Angot, P., Bruneau, C. H. and Fabrie, P. (1999). A penalisation method to take into account obstacles in viscous flows. *Numer. Math.* **81**, 497-520.

Berg, A. M. and Biewener, A. A. (2010). Wing and body kinematics of takeoff and landing flight in the pigeon (*Columba livia*). *J. Exp. Biol.* **213**, 1651-1658.

Bomphrey, R. J., Lawson, N. J., Taylor, G. K. and Thomas, A. L. R. (2006). Application of digital particle image velocimetry to insect aerodynamics: measurement of the leading-edge vortex and near wake of a Hawkmoth. *Exp. Fluids* **40**, 546-554.

Burrows, M. (2003). Biomechanics: froghopper insects leap to new heights. *Nature* **424**, 509.

Burrows, M. (2009). Jumping strategies and performance in shore bugs (Hemiptera, Heteroptera, Saldidae). *J. Exp. Biol.* **212**, 106-115.

Burrows, M. (2012). Jumping mechanisms in jumping plant lice (Hemiptera, Sternorrhyncha, Psyllidae). *J. Exp. Biol.* **215**, 3612-3621.

Card, G. and Dickinson, M. (2008). Performance trade-offs in the flight initiation of *Drosophila*. *J. Exp. Biol.* **211**, 341-353.

Clyne, J., Mininni, P., Norton, A. and Rast, M. (2007). Interactive desktop analysis of high resolution simulations: application to turbulent plume dynamics and current sheet formation. *New J. Phys.* **9**, 301.

Earls, K. D. (2000). Kinematics and mechanics of ground take-off in the starling *Sturnis vulgaris* and the quail *Coturnix coturnix*. *J. Exp. Biol.* **203**, 725-739.

Finn, J., Carlsson, J., Kelly, T. and Davenport, J. (2012). Avoidance of headwinds or exploitation of ground effect – why do birds fly low? *J. Field Ornithol.* **83**, 192-202.

Heppner, F. H. and Anderson, J. G. T. (1985). Leg thrust important in flight take-off in the pigeon. *J. Exp. Biol.* **114**, 285-288.

Kolomenskiy, D. and Schneider, K. (2009). A Fourier spectral method for the Navier–Stokes equations with volume penalization for moving solid obstacles. *J. Comput. Phys.* **228**, 5687-5709.
Kolomenskiy, D., Moffatt, H. K., Farge, M. and Schneider, K. (2011). Two- and three-dimensional numerical simulations of the clap–fling–sweep of hovering insects. *J. Fluids Struct.* **27**, 784-791.
Marden, J. H. (1987). Maximum lift production during takeoff in flying animals. *J. Exp. Biol.* **130**, 235-258.
Pekurovsky, D. (2012). P3DFFT: a framework for parallel computations of Fourier transforms in three dimensions. *SIAM J. Sci. Comput.* **34**, 192-209.
Pekurovsky, D. (2013). Parallel three-dimensional fast Fourier transforms (P3DFFT) library. San Diego Supercomputer Center (SDSC), available at http://code.google.com/p/p3dfft.
Provini, P., Tobalske, B. W., Crandell, K. E. and Abourachid, A. (2012). Transition from leg to wing forces during take-off in birds. *J. Exp. Biol.* **215**, 4115-4124.
Rayner, J. M. V. (1991). On the aerodynamics of animal flight in ground effect. *Philos. Trans. R. Soc. B* **334**, 119-128.
Rüppell, G. (1975). *Bird Flight.* New York, NY: Van Nostrand Reinhold.
Sunada, S., Kawachi, K., Watanabe, I. and Azuma, A. (1993). Performance of a butterfly in take-off flight. *J. Exp. Biol.* **183**, 249-277.
Takahashi, H., Tanaka, H., Matsumoto, K. and Shimoyama, I. (2012). Differential pressure distribution measurement with an MEMS sensor on a free-flying butterfly wing. *Bioinspir. Biomim.* **7**, 036020.
Tanida, Y. (2001). Ground effect in flight (birds, fishes and high-speed vehicle). *JSME Int. J. Ser. B* **44**, 481-486.
Tobalske, B. W., Altshuler, D. L. and Powers, D. R. (2004). Take-off mechanics in hummingbirds (Trochilidae). *J. Exp. Biol.* **207**, 1345-1352.
Walker, S. M., Thomas, A. L. R. and Taylor, G. K. (2009). Photogrammetric reconstruction of high-resolution surface topographies and deformable wing kinematics of tethered locusts and free-flying hoverflies. *J. R. Soc. Interface* **6**, 351-366.
Walker, S. M., Thomas, A. L. R. and Taylor, G. K. (2010). Deformable wing kinematics in free-flying hoverflies. *J. R. Soc. Interface* **7**, 131-142.
Zabala, F. A., Card, G. M., Fontaine, E. I., Dickinson, M. H. and Murray, R. M. (2009). Flight dynamics and control of evasive maneuvers: the fruit fly's takeoff. *IEEE Trans. Biomed. Eng.* **56**, 2295-2298.

Errata

"Force balance in the take-off of a pierid butterfly: relative importance and timing of leg impulsion and aerodynamic forces"

by G. Bimbard, D. Kolomenskiy, O. Bouteleux,
J. Casas and R. Godoy-Diana

JEB 216, 3551-3563

April 5, 2014

Equation (6) should read:

$$m\frac{d^2x_{\mathrm{cg}}}{dt^2} = F_{\mathrm{ax}}^{\mathrm{ns}}, \qquad m\frac{d^2z_{\mathrm{cg}}}{dt^2} = F_{\mathrm{az}}^{\mathrm{ns}} - mg, \tag{6}$$

Equation (7) should read:

$$F_{\mathrm{lx}} = [L_{\mathrm{l}} - z_{\mathrm{cg}}(t) + z_{\mathrm{cg}}(t_{\mathrm{l}})]K_{\mathrm{l}}\cos\phi_{\mathrm{l}}, \tag{7}$$

$$F_{\mathrm{lz}} = [L_{\mathrm{l}} - z_{\mathrm{cg}}(t) + z_{\mathrm{cg}}(t_{\mathrm{l}})]K_{\mathrm{l}}\sin\phi_{\mathrm{l}},$$

$$\text{if} \quad L_{\mathrm{l}} - z_{\mathrm{cg}}(t) + z_{\mathrm{cg}}(t_{\mathrm{l}}) > 0,$$

Equation (8) should read:

$$m\frac{d^2x_{\mathrm{cg}}}{dt^2} = F_{\mathrm{ax}}^{\mathrm{ns}} + F_{\mathrm{lx}}, \qquad m\frac{d^2z_{\mathrm{cg}}}{dt^2} = F_{\mathrm{az}}^{\mathrm{ns}} + F_{\mathrm{lz}} - mg, \tag{8}$$